machines

MDPI

Article

Lagrangian Simulation of Sediment Erosion in Francis Turbines Using a Computational Tool in Python Coupled with OpenFOAM

Mateo Narváez [1,2], Jeremy Guamán [1], Víctor Hugo Hidalgo [1,2,3], Modesto Pérez-Sánchez [4,*] and Helena M. Ramos [5]

[1] Laboratorio de Mecánica Informática, Escuela Politécnica Nacional (EPN), Quito 170517, Ecuador; mateo.narvaez@epn.edu.ec (M.N.); jeremy.guaman@epn.edu.ec (J.G.); victor.hidalgo@epn.edu.ec (V.H.H.)
[2] Departamento de Ingeniería Mecánica, Escuela Politécnica Nacional (EPN), Quito 170517, Ecuador
[3] Carrera de Pedagogía Técnica de la Mecatrónica, Facultad de Filosofía, Letras y Ciencias de la Educación, Universidad Central del Ecuador (UCE), Quito 170129, Ecuador
[4] Hydraulic Engineering and Environmental Department, Universitat Politècnica de València, 46022 Valencia, Spain
[5] Civil Engineering Research and Innovation for Sustainability (CERIS), Instituto Superior Técnico, Department of Civil Engineering, Architecture and Environment, University of Lisbon, 1049-001 Lisbon, Portugal; hramos.ist@gmail.com
* Correspondence: mopesan1@upv.es

Abstract

Hydraulic erosion from suspended sediment is a major degradation mechanism in Francis turbines of sediment-laden rivers, especially in Andean hydropower plants. This study presents a Python3.9-based computational tool integrating the empirical Oka erosion model within a Lagrangian particle tracking framework, coupled to single-phase CFD in OpenFOAM 10. The novelty lies in a reduced-domain approach that omits the spiral casing and replicates its particle-induced swirl via a custom algorithm, lowering meshing complexity and computational cost while preserving erosion prediction accuracy. The method was applied to a full-scale Francis turbine at the San Francisco hydropower plant in Ecuador (nominal discharge 62.4 m^3/s, rated output 115 MW, rotational speed 34.27 rad/s), operating under volcanic and erosive sediment loads. Maximum erosion rates reached ~1.2×10^{-4} mm^3/kg, concentrated on runner blade trailing edges and guide vane pressure sides. Impact kinematics showed most collisions at near-normal angles (85°–98°, peak at 92°) and 6–9 m/s velocities, with rare 40 m/s impacts causing over 50× more loss than average. The workflow identifies critical wear zones, supports redesign and coating strategies, and offers a transferable, open-source framework for erosion assessment in turbines under diverse sediment-laden conditions.

Keywords: CFD; hydraulic erosion; Francis turbines; solid particles; Oka model; Lagrangian simulation; Python; OpenFOAM

Academic Editors: Ali Khalfallah, Carlos Leitao and Elango Natarajan

Received: 8 July 2025
Revised: 9 August 2025
Accepted: 14 August 2025
Published: 15 August 2025

Citation: Narváez, M.; Guamán, J.; Hidalgo, V.H.; Pérez-Sánchez, M.; Ramos, H.M. Lagrangian Simulation of Sediment Erosion in Francis Turbines Using a Computational Tool in Python Coupled with OpenFOAM. *Machines* **2025**, *13*, 725. https://doi.org/10.3390/machines13080725

1. Introduction

Globally, hydropower generation stands as one of the most significant renewable energy sources, contributing approximately 14% to total electricity production. In South America, its share exceeds 45%, consolidating its position as a pillar of the regional energy matrix [1,2]. In countries with mountainous geography and abundant water resources, such as Ecuador, the hydroelectric infrastructure plays a strategic role within the national energy system [3].

In this context, Francis turbines have been widely adopted due to their ability to operate efficiently on a wide range of flow rates and net heads [4]. However, in numerous hydroelectric plants located in the Andean region, these turbines face adverse operating conditions due to the high load of mineral sediments transported by rivers. Such sediments are the result of natural processes such as surface erosion, geological instability, and the characteristic volcanic activity of the area [5].

The phenomenon of suspended solid particles constantly present in the flow induces hydraulic erosion. This progressive damage affects the internal surfaces of the turbine, especially the guide vanes, runner, and suction tube. Such wear compromises structural integrity and reduces system efficiency. It also increases corrective maintenance costs and leads to unplanned outages [6,7].

The severity of sediment-induced erosion is influenced by factors such as particle impact velocity and angle, particle size, hardness, concentration, and the material properties of the affected surface [8]. To quantify these effects, the model proposed by Oka et al. stands out for its high agreement with experimental data and its suitability for turbulent flow conditions and metallic material wear prediction [9,10]. Recent research has further validated and extended the Oka model for diverse applications, including complex three-phase flows [11], wind-driven gravel erosion of concrete [12], and sediment erosion in Francis turbines [13–15], demonstrating its continued relevance in 2025.

Advances in computational fluid dynamics (CFD) have enabled the integration of such models into detailed simulations of liquid–solid multiphase flows in hydraulic turbomachinery [16,17]. The Lagrangian particle tracking approach, often in a one-way coupling scheme, enables the prediction of erosion-prone regions with reasonable computational cost while preserving physical accuracy [18]. Recent studies have successfully coupled CFD with the Oka model to analyze erosion in industrial elbows [11], in high-head Francis turbines [14], in Himalayan sediment-laden hydropower plants [15], and even with enhanced formulations that account for non-spherical particles and variable granulometry [17].

Despite these advances, most works focus on specific industrial contexts (pipelines, concrete structures, Himalayan and Asian hydroelectric plants) with limited transferability to other hydrographic and sedimentological environments. There is a lack of studies applying this methodology to South American hydropower facilities, particularly in Ecuador, because the sediment characteristics and operational regimes differ significantly from previously reported cases. Moreover, while some recent approaches explore hybrid methods incorporating machine learning to improve predictive accuracy [12], the development of open, adaptable, and regionally calibrated computational tools remains a gap in the literature.

The novelty of this work lies in integrating mesh optimization, validated hydrodynamic predictions, and erosion modeling into a single workflow applied to a full-scale 115 MW Francis turbine under actual sediment-laden operating conditions. The workflow is implemented in OpenFOAM with customized Python-based post-processing to compute erosion rates using the Oka model. A dedicated Python module was developed to perform particle impact analysis through a Lagrangian approach, record impact conditions, and estimate local erosion. To reduce computational cost without compromising accuracy, the spiral casing was excluded from the mesh, and its effect on particle rotational motion was reproduced numerically. This integration enables accurate erosion prediction at a significantly lower cost, making it feasible to incorporate erosion assessment into early hydraulic design and maintenance planning without relying on commercial software.

As a case study, the methodology is applied to the San Francisco hydroelectric plant in eastern Ecuador, a facility reporting recurrent erosion damage under high gate-opening conditions. The proposed approach is open, reproducible, and adaptable, offering a framework for erosion assessment in hydraulic turbines operating under challenging sediment-laden flows and contributing transferable knowledge for similar hydrographic contexts worldwide.

2. Theoretical Foundations

The phenomenon of solid particle erosion in hydraulic turbomachinery is a surface degradation process caused by repeated impact of suspended mineral particles on metallic components under turbulent flow conditions [19,20]. This fluid–solid interaction leads to progressive material removal, altering the functional geometry of runner blades, guide vanes, and draft tube surfaces. In Francis turbines, such deterioration reduces hydraulic efficiency, increases operational costs, and shortens service life [16,21]. Similar patterns have been documented in sediment-laden hydropower plants in the Himalayas [15], in the Yellow River basin [14], and in large-scale installations in South America [22], highlighting its global relevance.

The erosion mechanism depends on multiple interrelated factors: relative velocity of impact, angle of incidence, particle hardness and shape, and the mechanical properties of the impacted material [8,10]. High-load regimes in Francis turbines—particularly under high gate openings or partial-load operation—can intensify flow separation, recirculation, and stagnation zones, increasing both particle concentration and impact energy [7]. Comparable flow behaviors have been associated with concentrated wear in guide vane–runner interfaces [17] and in labyrinth seal regions [12], emphasizing the importance of accurately modeling particle–surface interactions for erosion prediction.

From a physical perspective, particle impacts can be classified into three main categories: (i) normal impacts, where the particle strikes the surface perpendicularly, causing localized plastic deformation and potential surface cracking; (ii) tangential impacts, where the particle slides along the surface, leading to wear through shearing, material removal, or micro-machining; and (iii) oblique impacts, which combine both effects and result in more severe damage paths due to accumulation of cyclic stresses as confirmed by CFD–Lagrangian analyses in sediment-heavy Himalayan flows [15,23] and in large Kaplan runners [11]. The severity of wear depends on the impact energy, frequency, and microstructure of the material [24].

Particle shape is another critical factor. Angular particles with low sphericity have sharp edges that intensify abrasive wear. In contrast, rounded particles tend to cause less damage, although they may penetrate deeper into the flow domain [10,24]. This finding aligns with observations in silt-rich Andean rivers, where angular mineralogy is prevalent [20]. Likewise, the relative hardness between the particle and the base material (ASTM A743 grade CA6NM steel) determines the cutting capability: if the particle is significantly harder, such as quartz against stainless steel, the wear progresses more rapidly, even at low relative velocities [25]. In the present case, the Francis runner manufactured by VATECH in Hwaseong si, Gyeonggi do, South Korea uses this material, which is known for its good resistance to cavitation and erosion but remains susceptible to accelerated wear under high quartz content and angular sediment conditions.

At the macroscopic level, the operating conditions of the turbine influence the distribution and concentration of particles in the flow. Under partial load or hydraulic transients, the streamlines tend to become disordered, creating regions with a high probability of direct collisions [26]. Therefore, erosion is not uniformly distributed across internal surfaces, but is concentrated in specific regions whose identification is critical for predictive maintenance and geometric redesign [26,27].

Among empirical models for erosion prediction, the formulation by Oka et al. [10,28] remains one of the most widely adopted due to its robust validation against experimental data and adaptability to different particle types and material hardness values. Its volumetric erosion rate per unit particle mass, $E(\alpha)$, depends on the impact angle α, velocity v, particle diameter d, and the Vickers hardness Hv of the target material.

The general formulation of Oka's model adopts the following structure:

$$E(\alpha) = g(\alpha) * E_{90} \tag{1}$$

where $E(\alpha)$ represents the volume of material removed per unit mass of a particle at an impact angle α expressed in mm^3/kg; $g(\alpha)$ is the angular dependency function; and E_{90} is the volume removed at an impact angle of 90°.

The functions $g(\alpha)$ and E_{90} are defined as follows:

$$g(\alpha) = \left(sin(\alpha)\right)^{n_1} * \left(1 + H_v * \left(1 - sin(\alpha)\right)\right)^{n_2} \tag{2}$$

$$E_{90} = K_0 * (a * H_v)^{k_1 * b} * \left(\frac{v}{V'}\right)^{k_2} * \left(\frac{d}{D'}\right)^{k_3} \tag{3}$$

In this formulation, k_2 and k_3 are the exponents associated with the impact velocity and particle diameter, respectively. The coefficients n_1 and n_2 correspond to the parameters that determine the influence of the impact angle on the erosion rate. The variables D' and V' are standardization constants used to normalize the model's output [9,16].

The first term, $\left(sin(\alpha)\right)^{n_1}$, is associated with repeated plastic deformation or brittle fracture (depending on the value of n_1). The second term, $\left(1 + H_v\left(1 - sin(\alpha)\right)\right)^{n_2}$, represents the cutting action, which is more pronounced at shallow angles (grazing impacts). This reflects the mixed nature of erosion damage: both cutting and impact mechanisms [10].

A key advantage of the Oka model is its ease of integration into Lagrangian CFD frameworks, enabling erosion to be computed locally at each recorded impact [29]. This approach has been used in OpenFOAM-based studies for sediment erosion in Pelton injectors [12], high-head Francis runners [15], and silt-laden draft tubes [13], with results showing strong agreement with field inspections.

Implementing the model requires precise tracking of the impact position, the particle's relative velocity, its angle of incidence, and the associated mass or energy [10]. When collected across millions of impacts, this dataset enables the construction of detailed erosion maps and the identification of critical wear zones. As a result, it is possible to assess how operating or geometric conditions influence the life expectancy of components [30].

In summary, by coupling a detailed physical characterization of erosion mechanisms with insights from recent applied studies, and by implementing the validated Oka formulation within an optimized Lagrangian framework, this work advances and expands the current state of erosion modeling in sediment-laden hydropower systems. The combination of proven empirical modeling with strategies to reduce computational costs not only meets operational constraints but also delivers transferable and reproducible methodologies for broader application.

3. Materials and Methods

This methodology was designed to spatially predict erosion caused by solid particles in a Francis turbine (VATECH in Hwaseong si, Gyeonggi do, Republic of Korea) operating under real flow rate and load conditions. This study employs a one-way coupled computational approach, linking the hydraulic simulation of the carrier flow using

OpenFOAM with Lagrangian tracking of solid particles through an in-house-developed, Python-based too. The local erosion rate was calculated using the empirical model proposed by Oka, which was directly implemented in the Python tool based on the kinematic data obtained at each particle impact.

3.1. Geometric Simplification of the Domain

A significant challenge in turbomachinery simulation is the computational burden of fully resolving complex geometries, particularly the volute. Although this region is essential for capturing and channeling flow into the corridor, it presents a complex geometry with multiple curvatures, peripheral inflows, and local refinement requirements that significantly increase the number of mesh cells and, consequently, simulation time. To address this limitation, an alternative geometric simplification strategy is proposed, based on removing the volute from the computational domain and replacing it with an equivalent vectorial inlet condition that replicates its hydrodynamic effect [31].

The volute is replaced by a custom boundary condition. This is imposed on an artificial plane positioned at the runner's inlet. On this surface, a vector velocity field is imposed using the codedFixedValue condition, configured to generate a set of vectors radially oriented toward the runner's axis, with an adjusted inclination to represent the inflow pattern that would be induced by the actual spiral casing. This synthetic field reproduces the momentum and general direction of the incoming flow without requiring resolution of the internal geometry of the volute [32]. In Figure 1, the geometry of the Francis turbine is presented with the component that will be removed (volute).

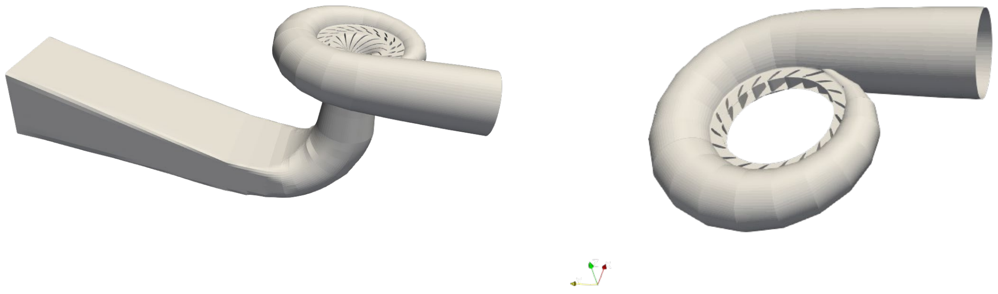

(**a**) (**b**)

Figure 1. Francis turbine geometry: (**a**) full assembly; (**b**) volute component (excluded in the simulation to reduce computational cost). Key dimensions: runner inlet diameter = 1530.8 mm; number of runner blades (Zb) = 13; guide vane height = 540.4 mm; number of guide vanes = 20; number of stay vanes = 20 [16].

This approach offers a key benefit: it drastically reduces the computational domain. This simplification reduces the cell count, accelerates mesh generation, and enables efficient execution of iterative or parametric studies, without compromising local hydrodynamic accuracy in the region of interest.

3.2. Geometric Modeling and Boundary Conditions

A representative geometry of the Francis turbine from the San Francisco hydropower plant (Ecuador) was used, modeled from 3D scans of the runner–distributor assembly. The simulated domain corresponds to the interior of the runner of a Francis-type turbine, isolated from other hydraulic components such as the spiral casing or draft tube. Mesh discretization was performed using snappyHexMesh, applying local refinement to the surfaces of interest (runner blades and walls) and incorporating prismatic layers to better capture near-wall gradients [33].

The fluid domain was discretized using the snappyHexMesh mesh generator, starting from an initial structured mesh defined through blockMesh with cubic geometry. The final mesh was generated based on an STL file containing multiple regions representative of the physical domain, including the erosion analysis surfaces (blades runner, blades guide), twenty radially distributed inlet ports (inlet 1–inlet 20), and rigid boundary surfaces (walls, draft out).

To accurately capture the solid–fluid interfaces and relevant geometric details, the castellated, snap, and addLayers meshing phases were enabled. In particular, mesh refinement with the insertion of prismatic layers (two layers) was applied on solid surfaces to improve the resolution of boundary conditions and shear stress gradients. Furthermore, the feature detection adjustment (featureSnapping) was activated using *.obj* files with marked edges, by setting the parameter explicitFeatureSnap *true*, in order to preserve critical geometric features. This configuration ensures an accurate representation of curved regions, sharp edges, and geometric transitions, guaranteeing mesh fidelity in complex hydraulic components [34,35].

Figure 2 provides a clear representation of the simplified turbine's geometry, which serves as the basis for the simulation setup.

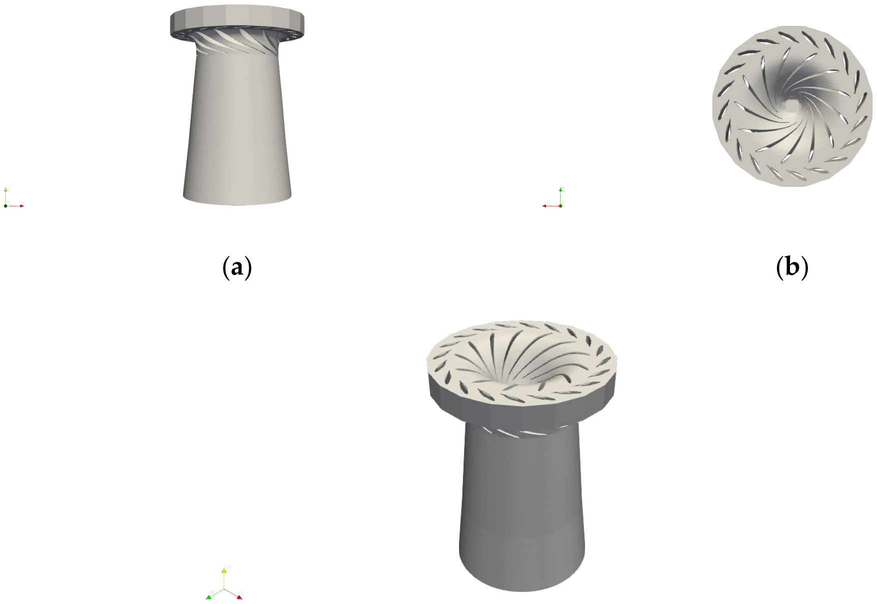
(**a**) (**b**)

(**c**)

Figure 2. Simplified geometry of the turbine used in the simulation: (**a**) side view; (**b**) top view; (**c**) isometric view.

To accurately simulate the particle impact erosion process, a one-way Eulerian–Lagrangian coupling strategy was adopted between fluid dynamics and solid particle dynamics. This approach decouples the solution of the velocity field from the particle trajectory calculation, under the assumption that the particles do not significantly alter the flow field. This approximation is valid in dilute particulate regimes, where the total mass of the particles is small compared to that of the carrier fluid [36,37].

The methodology was structured in two stages:

First stage: Solution of the fluid velocity field.

The steady-state velocity field of the carrier fluid (water) was solved using the simpleFoam solver from OpenFOAM, which implements the incompressible steady-state Navier–Stokes equations for turbulent flow. The RNG k–ε turbulence model was selected for its ability to capture recirculation and flow separation. It also accounts for local shear stress anisotropies, which are typical in curved hydraulic components [38]. Convergence was verified by monitoring residuals (threshold of 10^{-5}) and the stability of global quantities, such as mean pressure.

Second stage: Particle injection and erosion simulation.

Once the velocity field was obtained, the denseParticleFoam solver was used to resolve the Lagrangian transport of solid particles in the flow. The particle trajectories were integrated using Newton's equation of motion, considering drag forces, gravity, and collisions. Feedback from particles to fluid was not considered, which is a valid assumption in dilute regimes [39]. In addition, the Oka erosion model was activated to estimate the local mass loss on impact surfaces.

This type of coupling is widely used in erosion simulations in turbomachinery, as it significantly reduces computational cost compared to fully coupled models, without compromising accuracy in dilute particle regimes. However, in situations involving high concentrations of particles or local accumulation, bidirectional or fully coupled approaches are recommended [40].

3.3. Numerical Simulation

3.3.1. Physical Conditions and Flow Model

The flow simulation was carried out using a single-phase approach, assuming an incompressible and turbulent regime, since characteristic fluid velocities and system geometry rule out compressibility effects. Turbulence was modeled using Reynolds-Averaged Navier–Stokes (RANS) equations with the standard k–ε model. The turbulence resolution was activated by setting the turbulence parameter *on* in the configuration file. This model is widely used in internal flows and has shown a good performance in predicting recirculation and flow separation in hydraulic geometries [41].

The physical properties of the fluid (water) were set as constants, with a kinematic viscosity of $\upsilon = 1 \times 10^{-6}$ m^2/s and a density of $\rho = 1000$ kg/m^3, corresponding to standard ambient temperature conditions.

To simulate runner rotation without employing a moving mesh, a Multiple Reference Frame (MRF) scheme was implemented. This was defined over a central cylindrical region (mrfZone) of the domain, treated as a separate cellZone, in which a constant angular velocity was imposed. The rotation speed was set to $\omega = -34.271634$ rad/s, applied along the positive Y-axis direction. This approach allows for efficient representation of the interaction between stationary flow and moving components, while maintaining a static simulation domain and significantly reducing computational cost compared to moving mesh methods (ALE or sliding mesh) [42].

3.3.2. Carrier Flow Simulation

The flow of the carrier fluid (water) was resolved in the first stage of the one-way coupling using the simpleFoam solver, which is suitable for steady-state, incompressible and turbulent flow simulations. The RNG k–ε turbulence model was used due to its robustness and its ability to capture flow separation phenomena in complex geometries [38,43]. This configuration allows for the generation of a stabilized flow field that subsequently serves as the basis for the Lagrangian transport of solid particles.

The boundary conditions for the hydrodynamic variables are summarized in Table 1.

Table 1. Boundary conditions for the k-ε model.

Surface	U	p	k	Epsilon	Nut
Inlet	codedFixedValue	zeroGradient	fixedValue	fixedValue	calculated
Outlet	zeroGradient	fixedValue	zeroGradient	zeroGradient	calculated
Blades	movingWallVelocity	zeroGradient	kqRWallFunction	epsilonWallFuncion	calculated
Walls	zeroGradient	zeroGradient	kqrWallFunction	epsilonWallFunction	calculated

Boundary conditions were established based on controlled reference simulations, and a uniform inlet velocity of 30 m/s (U) was imposed, a value derived from previous erosion studies in the nozzles [30].

A noSlip boundary condition was applied at the domain walls to represent fluid adhesion to solid surfaces, allowing accurate resolution of the boundary layer. In addition, an equivalent surface roughness of 50 μm was defined to represent the texture of eroded steel.

For the initialization of turbulent kinetic energy (k) and turbulent dissipation rate (ε), a turbulence intensity of 5% (I) and a hydraulic diameter of 3 mm were assumed, typical values for high-speed nozzles. Based on the selected turbulence intensity and hydraulic diameter, the initial values of k and ε were calculated using the following equations.

Turbulent kinetic energy

$$k = \frac{3}{2}(U * I)^2 \tag{4}$$

Turbulent scale length

$$l = 0.07 * D \tag{5}$$

Turbulent dissipation rate

$$\varepsilon = \frac{C_\mu^{1/2} * k^{3/2}}{l} \tag{6}$$

The turbulent kinetic energy (k) was calculated as 3.375 m^2/s^2, while the turbulent length scale (l), based on the characteristic inlet diameter, was 2.1 × 10^{-4} m. From these values, the turbulent dissipation rate (ε) was determined to be approximately 4851.47 m^2/s^3, ensuring consistency with the selected turbulence model parameters and the physical characteristics of the incoming flow.

The inlet conditions were implemented using the fixedValue boundary type, while solid walls used wall functions (kqRWallFunction and epsilonWallFunction). Once numerical convergence was achieved, verified through residual thresholds, the velocity field, turbulent kinetic energy, and dissipation rate were exported in *.vtk* format to be used in Lagrangian particle simulation.

3.3.3. Particle Transport

Following stabilization of the velocity field, solid particle transport was simulated using the denseParticleFoam solver, part of the OpenFOAM library for Lagrangian simulations. The solver integrates Newton's second law for each particle in a non-interacting environment, accounting for forces such as drag, gravity, and wall collisions, without incorporating feedback from the particles to the fluid field.

The applicability of the one-way Eulerian–Lagrangian scheme was evaluated using the dimensionless loading parameter β. This parameter is defined as the ratio between the particle mass flow rate $\dot{m}_p$ and the carrier fluid mass flow rate $\dot{m}_f$, that is,

$$\beta = \frac{\dot{m}_p}{\dot{m}_f} \tag{7}$$

The parameter β quantifies the system's particulate loading. It serves as a standard criterion to determine whether the dispersed phase affects the continuous fluid phase. It must be verified that $\beta \leq 0.01$, which is within the accepted threshold in the literature, to justify the use of one-way coupling without significant loss of accuracy [42].

For $\beta \leq 0.01$, the influence of particles on the fluid velocity field is negligible, particularly in hydraulic engineering applications and erosion processes in dilute-phase regimes. Therefore, this simplification significantly reduces the computational cost without compromising the physical validity of the model [30].

The fluid mass flow rate was obtained from the expression $\dot{m}_{H_2O} = \rho * A * U$, where A is the cross-sectional area of the nozzle ($A = \pi * D^2/4$). Assuming a 1% particle loading, $\dot{m}_p = 0.01 * \dot{m}_{H_2O}$, leading to a resulting $\beta = 0.0099$. Since this value remains below the threshold of 0.01, the assumption of negligible particle-to-fluid feedback is valid within the dilute regime framework.

This result confirms that the fluid–particle interaction is weak enough to employ a unidirectional coupling scheme without compromising the validity of the model.

3.3.4. Particle Properties

The particles used in the simulation were spherical silicon oxide (SiO_2), a material commonly used in erosion studies due to its high hardness and thermal stability. Their physical properties, as reported by Cruzatty et al. [16], were a mean diameter of 100 μm and density of 2650 kg/m^3.

Based on these properties, the total number of particles injected during the simulation was estimated using the particle mass flow rate and the individual particle mass. The mass of a single spherical particle was estimated based on the diameter and the density, resulting in a volume of $5.24 \times 10^{-13} m^3$ and a corresponding mass of $1.39 \times 10^{-9} kg$. The number of particles injected per second was calculated as

$$N = \frac{\dot{m}_p}{m_p} \tag{8}$$

This results in an estimated injection rate of 1.53×10^6 particles per second under steady-state flow conditions. The selection of specific diameter and density values directly influences the particle impact kinetic energy and, therefore, the erosion rate, an essential factor for the model's accuracy.

3.3.5. Particle Simulation

Solid particle transport was simulated through a discrete Lagrangian approach using parcels, where each parcel represents a statistically equivalent group of particles. Injection was configured in the cloudProperties file using the patchInjection model. Each domain inlet (inlet 1 to inlet 20) was assigned a separate injection source. The total injection rate was set at 50,000 parcels per second, corresponding to SiO_2, commonly used in erosion experiments due to its high mass-to-volume ratio and its suitability to simulate moderate impact behavior [44]. The characteristics of the particles are summarized in Table 2.

Table 2. Summary of particles characteristics.

Characteristic	Unit	Value
Diameter	µm	100
Density	kg/m^3	2650
Injection rate	parcels/s	50,000

Only drag was considered in the motion model, implemented via the sphereDrag formulation, which is appropriate for moderate Reynolds numbers. For interactions with solid surfaces, the rebound model was activated, defining the post-impact behavior of the particle. The coefficients used were the restitution coefficient $e = 0.97$, indicative of a nearly elastic rebound, and the friction coefficient $\mu = 0.09$, responsible for tangential energy losses. Escape conditions were applied to all inlet and outlet surfaces, allowing particles that re-entered or exited the geometry to be removed from the simulation.

Interparticle collisions were not considered, which is consistent with the previously established dilute particle concentration regime. To account for damping effects in non-stabilized trajectories, the relaxation model was activated using the nonEquilibrium option, allowing for a more realistic transition toward dynamic equilibrium in the particle system.

This Lagrangian approach, combined with simplified interaction models and no fluid-phase feedback, is particularly efficient for dilute flows in complex geometries and is widely used for prediction of surface erosion in turbomachinery and hydraulic channels [10].

3.3.6. Numerical Configuration

The fluid field was solved using the simpleFoam solver from OpenFOAM, which is typically used for steady-state simulations but was adapted here in combination with a transient particle-coupled approach. To achieve this, the hybrid PIMPLE algorithm (SIMPLE + PISO) was applied. The number of outer correctors was set to 2, which improves numerical stability and convergence in simulations involving rotating domains and regions with strong gradients.

The numerical convergence tolerances were strictly set to 1×10^6 for the main flow variables: pressure (p), velocity (U), turbulent kinetic energy (k), and dissipation rate (ε), to ensure the stability of the solution and the high-quality field resolution.

The time control for the Lagrangian phase was defined using a constant time step of $\Delta t = 0.0001$ s, with a total simulation time of 5 s, which was sufficient to reach a steady-state particle flow regime within the domain. Results were recorded every 0.02 s, enabling high-temporal-resolution post-processing and stability monitoring through the Courant number.

3.3.7. Mesh Independence

In general, the accuracy of the results depends to a large extent on the computational domain. Usually, a higher element density yields more accurate results; however, this proportionally increases the calculation time in a numerical simulation. For this reason, it is important to determine the point at which the mesh element density no longer affects the simulation results, in order to optimize computational resources to the maximum while still obtaining reliable results.

Given the complexity of the computational domain used in this study, it is necessary to demonstrate that the optimization performed will not produce results that deviate from experimental values and previous findings. Hidalgo demonstrated that the computational domain resulting from the meshing technique used in his case study is independent of element density [45]. Based on this information, four meshes with different element densities will be developed, starting from a very fine mesh used by Velasco and progressing to an optimized mesh.

This will be determined by calculating the torque exerted on the turbine's moving blades at the point where the calculated values reach stability, using the SIMPLE algorithm. These data will make it possible to determine whether the predictions obtained through numerical simulation are independent of the number of mesh elements used.

As can be seen in Figure 3, all cases reach a stability value, obtaining the following results:

The optimized mesh (1.31 M cells) yields a power of 103.20 MW and an efficiency of 88.0%, corresponding to relative errors of 5.8% and 6.4%, respectively. The finest mesh (4.65 M cells) predicts 107.45 MW and 92.0% efficiency, with relative errors of 1.9% and 2.1%. These deviations are within the range typically reported for steady RANS simulations of Francis turbines in the literature.

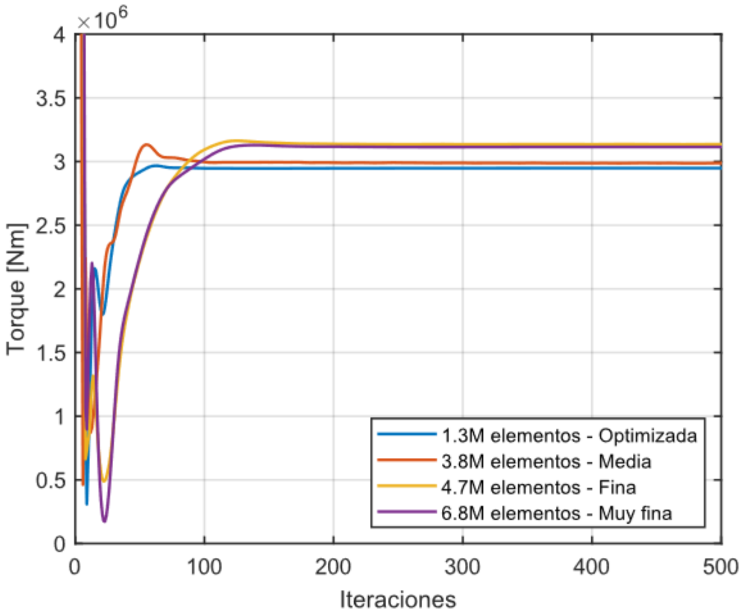

Figure 3. Torque values in different meshes.

Table 3 shows the torque, power, efficiency, error, and execution time values for different mesh models.

Table 3. Torque values for different meshes.

Model	Number of Elements	Torque [Nm]	Power [MW]	Efficiency	Error [%]	Run Time [h]
Experimental	-	-	109.50	0.94	0.0	-
Optimized	1 311 097	2 948 600	103.20	0.88	5.8	04h31
Medium 2	3 774 986	2 986 000	104.51	0.90	4.6	07h10
Fine	4 648 862	3 135 300	107.45	0.92	1.9	11h29
Very fine	6 795 222	3 114 500	106.74	0.91	2.5	19h01

3.3.8. Experimental Data Validation

The numerical predictions were validated using operational records from the San Francisco hydropower plant, equipped with a Francis turbine manufactured by VATECH, with a rated output of 115 MW, a nominal discharge of 53 m^3/s, and a rotational speed of 34.27 rad/s (clockwise from top view). Key operational parameters include a water temperature of 16 °C, density of 998.9 kg/m^3, and kinematic viscosity of 1.106×10^{-6} m^2/s.

Table 4 summarizes the plant registers for different operating points, including measured pressures upstream (P_1) and downstream (P_2) of the turbine, discharge (Q), electrical power output, hydraulic power, and calculated efficiency.

Table 4. Operational records and performance indicators of the San Francisco hydropower plant at different operating points.

Q [m^3/s]	P_1 [Pa]	P_2 [Pa]	Electrical Power [MW]	Hydraulic Power [MW]	Efficiency [%]
17.0	2,100,000	71,000	29.3	34.5	85
25.9	2,090,000	72,000	40.3	52.3	77
33.4	2,070,000	75,000	55.5	66.6	83
33.2	2,060,000	70,000	56.2	66.1	85
40.3	2,050,000	75,000	70.6	79.6	89
45.1	2,050,000	80,000	79.2	88.8	89
50.8	2,000,000	80,000	90.9	97.5	93
56.0	2,000,000	80,000	100.1	107.5	93
59.7	1,950,000	80,000	105.8	111.6	93
62.4	1,950,000	80,000	109.5	116.7	94

For the nominal operating point simulated (Q = 62.4 m^3/s, P_1 = 1.95 MPa, P_2 = 0.08 MPa), the measured electrical power is 109.50 MW, with an efficiency of 94.0%. Table 3 compares these values with the results obtained for four mesh densities, including the mesh-independent solution.

In addition to the quantitative validation, a qualitative comparison was carried out between the predicted erosion patterns and the actual wear observed in the runner and guide vanes during plant inspection. Figure 4 shows the erosion rate distribution computed with the Oka model (left) and the corresponding photographic evidence of the damaged surfaces (right). In both components, the highest simulated erosion intensities coincide spatially with the areas exhibiting the most severe material loss in the real turbine, particularly along the trailing edge of the runner blades and the pressure side of the guide vanes. This agreement in both magnitude and location supports the representativeness of the numerical model in reproducing the erosion mechanisms present under sediment-laden operating conditions.

(**a**) (**b**)

(**c**) (**d**)

Figure 4. Comparison between simulated erosion patterns using the Oka model and actual wear observed during plant inspection in the runner and guide vanes of the San Francisco hydropower plant: (**a**) numerical prediction of erosion in the runner; (**b**) photographic evidence of erosion in the runner; (**c**) numerical prediction of erosion on guide vanes; (**d**) photographic evidence of erosion on guide vanes.

3.3.9. Post-Processing

During simulation, several automated monitoring and analysis functions were activated through the controlDict file. Specifically, the hydrodynamic forces on the analysis surfaces (blade runners) were computed using the force function. Additionally, the solver recorded convergence residuals, the local y^+ value (as a mesh quality indicator near walls), the Courant number, and the second invariant of the velocity gradient tensor (Q-criterion), which is useful for visualizing vortex structures.

For erosion results, the field cloud:QOka corresponding to the erosion rates of the Oka model was exported. These datasets were prepared for analysis using external tools such as ParaView 5.9 (for 3D visualization) and Python, using PyVista v0.46.1 for spatial mapping and NumPy 2.3.2 for statistical analysis and erosion profiling.

This integrated post-processing strategy allows not only for the validation of fluid dynamics and particle evolution fields but also for high-resolution spatial and temporal analysis of surface wear.

3.4. Lagrangian Simulation Tool in Python

A Python numerical simulation tool was developed to perform Lagrangian tracking of solid particles based on steady-state flow fields obtained through CFD simulations. The purpose of the model is to evaluate the behavior of sediment particles under the operating conditions of a hydraulic turbine, considering both individual trajectories and potential interactions with the internal surfaces of the system.

The particles were injected on a defined surface upstream of the runner, with initial velocities that coincided with the surrounding flow. Spherical particles with a density of 2650 kg/m^3 and an average diameter of 100 μm were assumed, consistent with granulometric analyses of sediments from the Pastaza River [16]. Turbulent dispersion was modeled using a stochastic scheme in which random fluctuations were added to the interpolated velocity field.

3.4.1. Spatial Interpolation of the Velocity Field

To accurately simulate particle transport within a complex three-dimensional flow domain, it is essential to implement an effective method for interpolating the velocity field from a CFD simulation mesh to arbitrary locations in space. The proposed approach allows the use of an interpolation scheme based on K nearest neighbors (K-NN), inversely weighted by distance. This approach provides a continuous estimation of the fluid velocity vector over a set of moving Lagrangian points [46]. The adopted formulation was as follows:

$$\vec{v}(\vec{x}) = \frac{\sum_{i=1}^{K} \frac{1}{d_i + \varepsilon} \vec{v}_i}{\sum_{i=1}^{K} \frac{1}{d_i + \varepsilon}} \tag{9}$$

where $\vec{v}_i$ represents the fluid velocity at node i of the mesh, d_i is the Euclidean distance between the point of interest $\vec{x}$ and that node, and ε is a very small positive constant used to avoid division by zero when the distance is near zero.

This type of interpolation is well suited for complex domains with unstructured meshes, as it avoids artifacts introduced by simple linear schemes and improves the stability of the Lagrangian model. However, its accuracy critically depends on the local node density and the number of neighbors selected [47,48].

3.4.2. Temporal Integration of Movement

Particle motion was integrated using the explicit Euler method, which is widely used in Lagrangian dynamics because of its simplicity and low computational cost. This method allows the calculation of each particle's future position and velocity based on its current state and the forces acting upon it. The governing equations used were

$$\overrightarrow{v_{t+\Delta t}} = \overrightarrow{v_t} + \overrightarrow{a_t} \cdot \Delta t \tag{10}$$

$$\overrightarrow{x_{t+\Delta t}} = \overrightarrow{x_t} + \overrightarrow{v_{t+\Delta t}} \cdot \Delta t \tag{11}$$

where $\overrightarrow{a_t}$ is the total acceleration, composed of gravitational acceleration and fluid drag force; $\overrightarrow{v_t}$ is the current particle velocity; and Δt is the time step.

Due to its conditional stability, a small time step of Δt = 0.0001 was used. The simulation ran for 5 s to ensure accuracy and resolution. This scheme is appropriate, as the goal is to achieve a high temporal resolution in a scenario characterized by frequent collisions and intense dynamic interactions [49,50].

Once the velocity at each particle location was determined through spatial interpolation, the particle's velocity was updated using the explicit Euler scheme and the applied forces.

3.4.3. Drag Force: Schiller–Naumann Correlation

The interaction between the fluid and the particle was modeled through the drag force, which constitutes the primary mechanism for momentum exchange between the two phases. This force was defined on the basis of the classical Schiller–Naumann correlation, which is valid for spherical particles in laminar and transitional regimes with moderate Reynolds numbers.

$$\vec{F}_{drag} = \frac{1}{2} * C_d * \rho_f * A_p * |\vec{v}_{rel}| * \vec{v}_{rel} \tag{12}$$

where C_d is the drag coefficient, ρ is the fluid density, $A_P = \pi d^2/4$ is the projected area of the particle, and $\vec{v}_{rel}$ is the relative velocity between the particle and the fluid. The particle Reynolds number is defined as

$$Re_p = \frac{\rho_f * d * |\vec{v}_{rel}|}{\mu} \tag{13}$$

with μm being the dynamic viscosity of the fluid. Depending on Re_P, the following condition applies:

$$C_d = \begin{cases} \frac{24}{Re_p} * \left(1 + 0.15 * Re_p^{0.687}\right) & si \quad Re_p < 1000 \\ 0.44 & si \quad Re_p \geq 1000 \end{cases} \tag{14}$$

This correlation has been experimentally validated and is widely used in multiphase flow simulations [51,52].

3.4.4. Collisions with Solid Surfaces

Collisions were detected using a 3D KDTree spatial structure, constructed from mesh points on solid surfaces. This method enables efficient proximity queries in complex geometries.

When a collision is detected, the velocity of the particle is reflected with respect to the normal surface at the point of contact, simulating an elastic rebound [53]. This operation is modeled using the following expression:

$$\overrightarrow{v_{\text{new}}} = \vec{v} - 2 * (\vec{v} \cdot \hat{n}) * \hat{n} \tag{15}$$

where $\vec{v}_{rel}$ is the velocity prior to impact and $\hat{n}$ is the unit normal vector on the solid surface. To represent different energy restitution conditions during the collision, a restitution coefficient $\varepsilon \in [0,1]$, which modifies the magnitude of the reflected velocity depending on the nature of the particle–surface interaction.

This process is repeated until the total simulation time is completed, storing the trajectory of each particle for subsequent analysis and visualization. Model output enables identifying trajectory clusters, rebound zones, and areas prone to particle–surface wear.

Each surface collision modifies the particle's kinetic energy. The resulting impact conditions are then used to evaluate local erosion using the Oka model.

3.5. Erosion Calculation with the Oka Model

The formulation proposed by Oka et al. was adopted, which enables the evaluation of the volume eroded per unit mass of a particle under normal impact conditions (1), (2), and (3), using reference parameters and experimentally calibrated exponents for metallic materials [10].

The calibrated values of these parameters, which involve sand particles and stainless-steel surfaces, are detailed in Table 5.

Table 5. Parameters for the Oka model.

Parameter	Unit	Value
K_0	-	65
k_1	-	−0.12
k_2	-	2.36
k_3	-	0.19
n_1	-	0.78
n_2	-	1.27
a	-	0.0221
b	-	0.45
V'	m/s	104
D'	m	0.00326

The accumulated erosion results per cell were stored in *.vtk* format and visualized using ParaView, allowing the generation of three-dimensional maps of potential damage on the hydraulic surface.

3.6. Simulated Scenarios

Multiple simulations were carried out under different opening conditions of the runner (50%, 75%, and 100%) to evaluate the effect of the operating regime on the spatial distribution of erosion. For each case, between 10^5 and 10^6 particles were injected and several flow-equivalent seconds were simulated, allowing a statistically representative sampling of particle impacts.

The comparison between scenarios allowed for the identification of repetitive damage patterns, validation of hypotheses about critical zones, and estimation of the relative increase in erosion as a function of the inlet flow rate.

4. Results and Analysis

4.1. Consistency Verification Between Full and Reduced Domains

To validate the representativeness of the reduced geometric model, the pressure results on the runner were compared between two configurations of the computational domain. The first configuration included the complete domain comprising the spiral casing, guide vanes, runner, and draft tube. The second used a trimmed mesh restricted to the guide vanes, the runner, and a portion of the draft tube.

Figure 5 shows a comparison of pressure distribution (Pa) over the runner in both domain configurations: (a) Full domain including the spiral casing, guide vanes, runner, and draft tube. (b) Reduced domain including only the guide vanes, runner, and part of the draft tube.

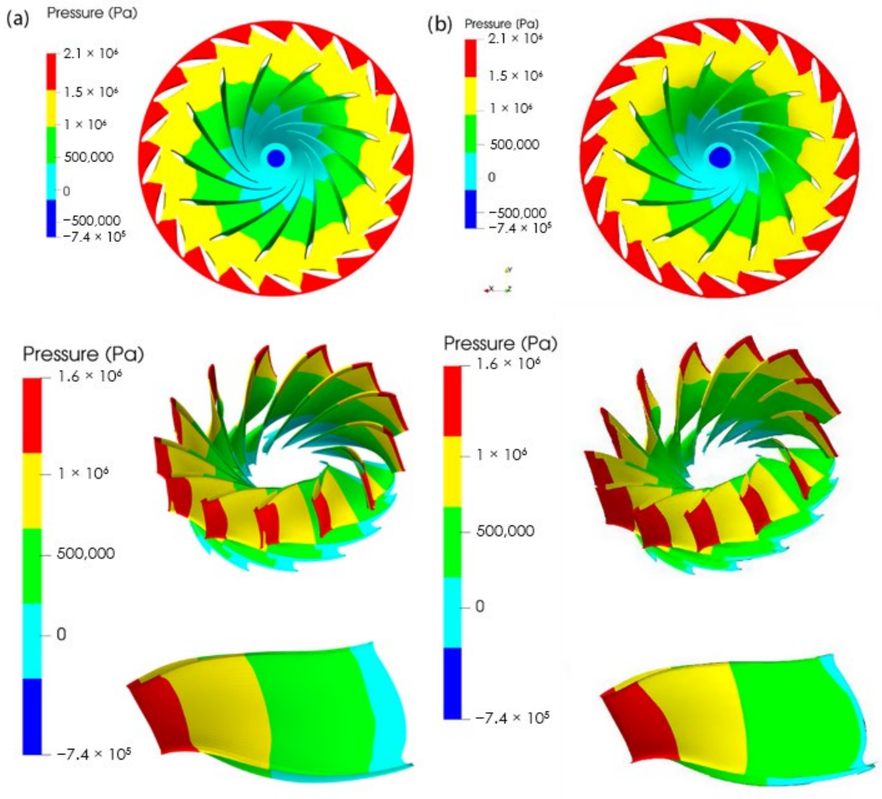

Figure 5. Pressure distribution over the impeller for two domain configurations: (**a**) full domain (cone, guide vanes, impeller, and suction pipe); (**b**) reduced domain (guide vanes, impeller, and a segment of the impeller).

The pressure distribution on the runner is shown to be equivalent in both cases, validating the use of the reduced domain for subsequent analyses.

4.2. Spatial Distribution of Erosion

Figure 6 shows the spatial distribution of the erosion rate on the surfaces of the guide vanes (left), along with the trajectories of the solid particles (right). The color scale represents the magnitude of the accumulated erosion per cell, expressed in mm^3/kg, as calculated using the Oka model. This value corresponds to the volume of material lost per kilogram of impact particles under local conditions of velocity, angle, and particle size.

Highly eroded regions (darker tones) are concentrated on the rear side of the guide vanes, particularly near the mid-upper portion of their height. This location coincides with the concentration of particle trajectories, suggesting a higher frequency of impacts in those areas. The right-hand image confirms this correlation, showing a dense bundle of trajectories intersecting the eroded zone perpendicularly, indicating incidence angles near those associated with maximum erosion according to the model.

The maximum erosion values reach approximately 1.2×10^{-4}, indicating that up to 120 microliters of material are lost per kilogram of suspended particles in the most critical zones. This is significant, as under real operating conditions, particulate flow can reach several kilograms per second, leading to substantial cumulative wear rates.

Figure 7 presents the spatial distribution of the erosion rate on the runner (left), along with the solid particle trajectories (right), calculated using a Lagrangian simulation. As with guide vanes, the color scale represents the eroded volume per unit of particle mass in mm^3/kg, according to the Oka model.

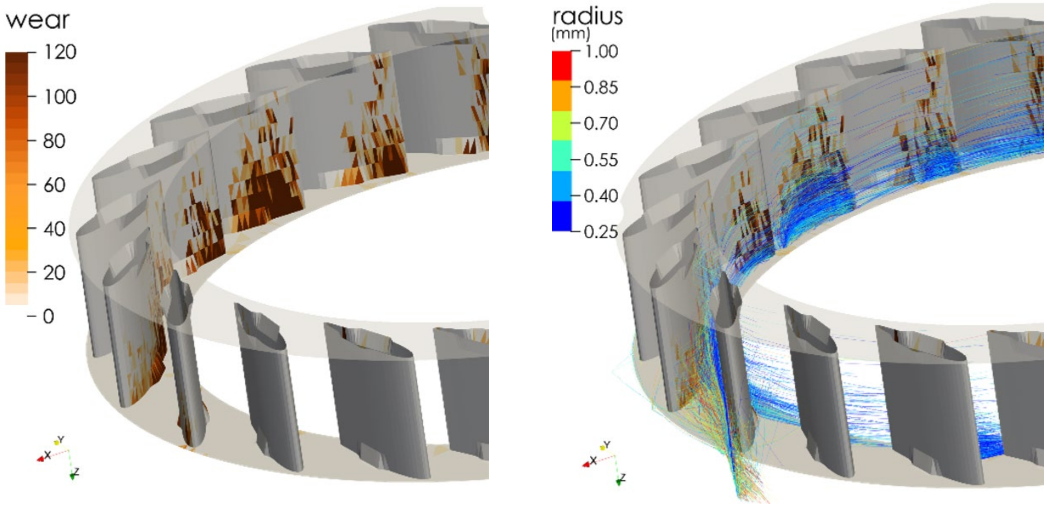

(**a**) (**b**)

Figure 6. Lagrangian simulation results on the guide vanes: (**a**) accumulated erosion rate; (**b**) particle trajectories.

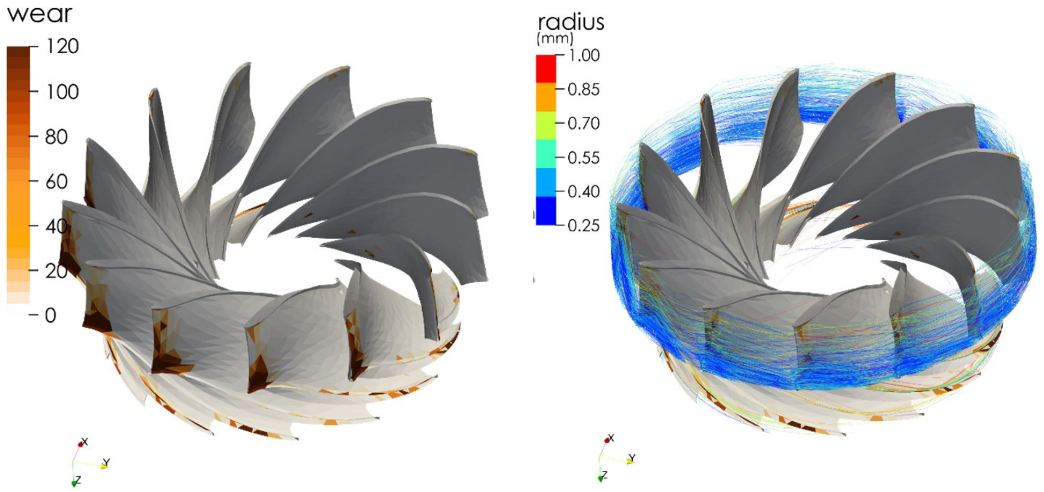

(**a**) (**b**)

Figure 7. Predicted erosion rate distribution (**a**) and particle trajectories colored by velocity magnitude (**b**). The outer ring exhibits denser trajectory visualization due to longer particle residence times. In the central hub region, particles pass through rapidly, and the applied opacity settings make their traces less visible despite their presence.

The visualization in Figure 7 shows a higher density of particle trajectories in the outer ring of the runner. This occurs because sediment particles tend to remain longer in that region before exiting, while their passage through the inner sections of the runner is brief. Although particles do enter the hub-side passages, their short residence time results in minimal visible traces under the opacity settings applied in the post-processing. These settings intentionally enhance the visibility of regions with a high particle residence time, highlighting areas more prone to sediment-induced wear.

The erosion is mainly concentrated in the runner outlet zone, particularly along the crown and band ring, with a predominance on the rear faces of the blades. This region corresponds to the passage of particles accelerated by the guide vanes and striking at intermediate to shallow angles conditions under which the model predicts high cutting efficiency and therefore greater volume loss.

The right-hand image shows a high density of trajectories intersecting these regions tangentially, reinforcing the correlation between impact pattern and observed wear.

These results allow for the identification of critical areas for potential hydraulic redesign or application of abrasion-resistant coatings, as well as the definition of operating strategies to minimize prolonged exposure to erosive conditions [16].

Figure 8 displays the spatial distribution of the erosion rate on both sides of the runner blades: rear face (top) and leading face (bottom). The results were obtained through Lagrangian simulation using the Oka model, which estimates volumetric loss per unit mass of impact particles (in mm^3/kg).

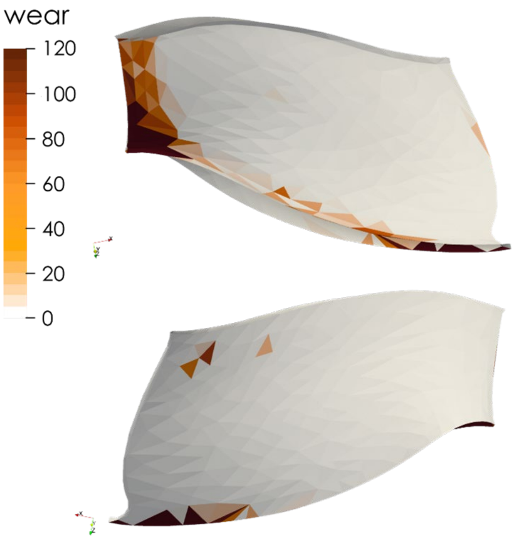

Figure 8. Surface distribution of erosion rate on the impeller blades.

The rear face of the blade shows higher levels of erosion, with pronounced concentrations near the trailing edge, particularly toward the upper and lower regions of the blade. These zones correspond to areas where the flow directs particles along trajectories that impact at medium angles and high relative velocity—conditions that maximize damage per model employed.

In contrast, the leading face exhibits considerably lower erosion levels, with a more diffuse and lower magnitude distribution. This aligns with the hydraulic behavior of Francis runners, where particles tend to follow streamlines and only occasionally impact the pressure side of the blade.

4.3. Impact Kinematics Statistics

4.3.1. Statistical Distribution of the Impact Angle

Figure 9 presents the distribution of impact angles recorded during the Lagrangian simulation of solid particles suspended in the hydraulic flow through a Francis turbine runner. Most of the impacts occurred within a narrow range between 85° and 98°, with a peak around 92°, indicating a strong tendency toward normal or near-normal collisions with blade surfaces.

The high erosion intensities observed near the trailing edge of the guide vanes and on the pressure side of the runner blades (Figure 7) are explained by the particle impact angle distribution shown in Figure 9. The dominant peak, between 85° and 100°, falls within the range of maximum erosion rate for ductile materials according to the Oka model, which explains the severe wear observed in both the numerical predictions and field inspections. The smaller peak near 150° is linked to reverse impacts produced by local flow recirculation zones, where particles are redirected toward the surface in the opposite direction of the main flow. Furthermore, the minor group of impacts below 40° in Figure 9 can be interpreted as mirror angles of the main impacts. These occur when particles strike surfaces oriented in the opposite direction, generating complementary impact geometries that still contribute to localized material removal.

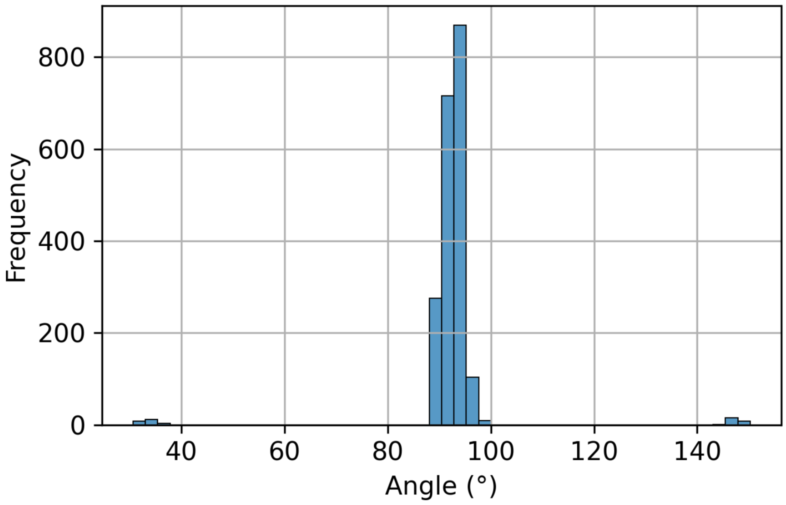

Figure 9. Statistical distribution of solid particle impact angles on impeller surfaces.

This behavior is consistent with applied CFD and real turbine studies, such as those by Cruzatty et al. and Shrestha et al., which show that under high sediment load conditions, particles tend to follow trajectories resulting in frontal collisions, especially near the trailing edge and suction side of the blades. According to the Oka model, widely used in similar contexts, this angular range corresponds to the maximum severity of erosion in brittle materials and still critical conditions in ductile materials such as turbine steels [16,54].

The near-zero frequency of low-angle impacts (<45°) suggests that particles are not grazing surfaces tangentially. Although this is favorable in terms of reducing friction, it may not reduce total erosion, as normal impacts are more likely to remove material via direct penetration or microfracture depending on impact velocity and relative hardness.

Some isolated cases with angles around 140° to 150° were identified, likely the result of reflected or recirculated trajectories. Although infrequent, such impacts can contribute to unexpected wear on the surface of the main blade or on the internal structure of the duct.

Overall, the distribution confirms that the simulated flow regime generates potentially aggressive conditions for structural materials in the runner, concentrating impacts in an angular range associated with high erosive efficiency per the Oka model and experimental evidence from sediment-laden hydraulic turbines.

4.3.2. Statistical Distribution of the Impact Velocities

Figure 10 shows the histogram of impact velocities for solid particles recorded in the CFD–Lagrangian simulation of internal flow through a Francis turbine. Most impacts occurred at velocities between 5 and 10 m/s, with a frequency peak around 5 m/s, typical conditions for sediment transport in moderate-flow regions of the runner or guide vanes.

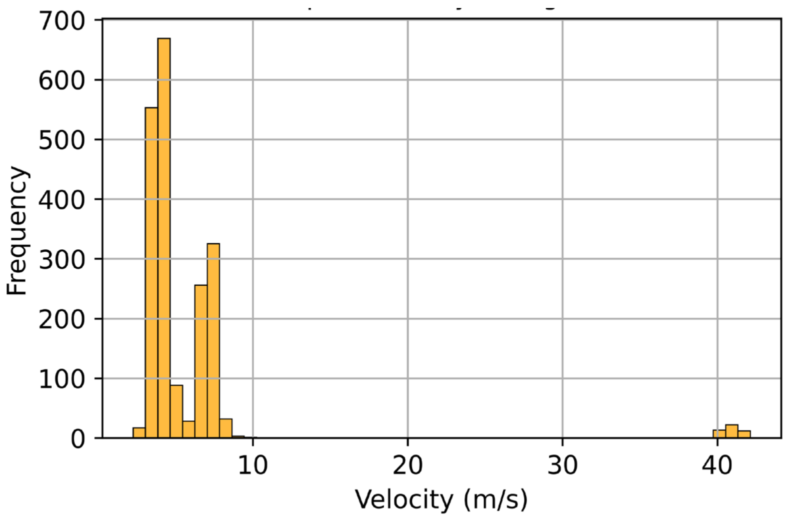

Figure 10. Histogram of particle impact velocities recorded during the simulation.

The distribution in Figure 10 shows two distinct clusters of particle impact velocities, one concentrated between 5 and 10 m/s and another near 40 m/s, with an absence of events in the intermediate range. This behavior is a consequence of the flow field inside the turbine. Particles that interact with blades, guide vanes, or low-energy recirculation zones rapidly decelerate and fall into the low-velocity group, while those travelling through the main high-energy channels maintain velocities close to the inlet until impact. The lack of intermediate values suggests that particles either lose a significant portion of their momentum almost immediately upon entering low-energy regions or preserve most of it until collision, with no gradual transition between the two states.

According to the Oka model, erosion E is proportional to impact velocity raised to an exponent k_2 (typically between 2.3 and 2.8 for metals), i.e., $E \approx v^{k_2}$. Consequently, an impact at 40 m/s may cause over 50 times more damage than one at 8 m/s.

This effect has been confirmed in both experimental and numerical studies. High-velocity impacts tend to concentrate in flow acceleration zones, such as runner trailing edges and narrow regions of the draft tube. These particles, carrying greater kinetic energy, cause intense localized erosion, especially when striking at oblique angles optimal for material removal [55–57].

5. Discussion

The results obtained in this study provide strong evidence regarding the erosion mechanisms that affect Francis turbines operating in solid particle-laden flows. The combined use of computational simulation with OpenFOAM and a customized Lagrangian model implemented in Python enabled the evaluation of wear severity on the runner and guide vanes with high spatial and statistical resolution. This section interprets the findings in the context of the specialized literature, examining their validity, technical implications, and possible limitations.

5.1. Comparison Between Full and Reduced Domains

One of the initial methodological decisions evaluated was the simplification of the geometric domain. By comparing the simulation that includes the spiral casing, guide vanes, runner, and draft tube with a reduced domain consisting only of the guide vanes, runner, and a portion of the outlet tube (Figure 5), it was observed that the pressure distributions on the runner were virtually identical. This equivalence validates the use of the reduced domain for particle impact studies. It significantly reduces computational requirements while maintaining the accuracy of the pressure field and facilitates parametric simulations at lower operational costs.

This approach is consistent with the findings of Montomoli et al. (2011), who demonstrated that inlet conditions can be effectively represented using synthetic velocity profiles [32]. Likewise, Arocena and Danao (2023) highlighted the viability of this type of geometric reduction in multiphase flow studies when the focus is on the runner without compromising analytical quality [31].

5.2. Spatial Distribution of Erosion and Correlation with Trajectories

The erosion maps on the guide vanes (Figure 6) and the runner (Figure 7) show that the highest material loss is concentrated at the trailing edges of the blades. In particular, significant wear is observed on the rear face and trailing edges near the crown and band ring. This distribution is explained by the acceleration of the flow and the orientation of the particle trajectories, which direct the particles toward these surfaces with angles close to a normal incidence.

This pattern aligns with observations by Cruzatty et al. (2022), who reported that regions near the trailing edge of the blades experience a higher concentration of impacts and wear [16]. In these areas, the two-phase flow accelerates, changes direction, and guides the particles toward vulnerable metallic surfaces, causing kinetic energy accumulation, concentrated impact, and localized damage.

The particle trajectories, overlaid in the figures, clearly demonstrate spatial coincidence between regions of high impact density and areas of greatest erosion. This correlation validates the accuracy of the developed Lagrangian method and supports the use of the Oka model in hydro-turbomachinery contexts.

5.3. Impact Angle and Velocity Statistics

The impact angle distribution (Figure 9) shows a peak around 92°, indicating a predominance of almost perpendicular impacts. This type of collision generates greater wear in medium-hardness metals commonly used in hydraulic components, as determined by Oka et al. [10]. Perpendicular impacts tend to produce micro-cutting, surface micro-fracture, and localized material removal [10].

The velocity distribution (Figure 10) shows a trend centered between 6 and 9 m/s, but isolated high-velocity events above 30 m/s were also detected. Although infrequent, these high-speed collisions contribute significantly to cumulative damage. The Oka model applies a non-linear exponent ($k_2 \approx 2.36$) to the velocity, amplifying the erosive effect of such events.

Studies by Thapa et al. [8] and Fortini et al. [25] demonstrate that even small increases in velocity can lead to significant increases in wear rate. This relationship highlights the importance of optimizing hydraulic profile design to reduce zones of abrupt acceleration, minimize turbulence near solid surfaces, and avoid alignments that favor high-kinetic-energy impacts [8,25].

5.4. Applicability of the Oka Model and Engineering Considerations

The Oka model has proven to be suitable for estimating erosion caused by solid particles under realistic hydrodynamic conditions. It accounts for the effects of the impact angle, velocity, diameter, and mass of the particle. The model output in mm^3 of loss per kilogram of particles allows the estimation of cumulative wear volumes, the calculation of loss rates over time, and the projection of component lifetime.

Its integration into a Python-based tool coupled with OpenFOAM results enabled a detailed evaluation of wear in actual turbine geometries. The tool facilitated the detection of vulnerable areas, a comparison between scenarios, and the establishment of hydraulic redesign criteria.

The methodology developed allows erosion analysis under different operating conditions. It also enables the comparison of alternative designs and the evaluation of mitigation strategies, such as abrasion-resistant coatings, thermal treatments, or modifications in blade geometry.

6. Conclusions

This study successfully demonstrated a coupled simulation approach—integrating OpenFOAM with a customized Lagrangian particle tracking model—for evaluating erosion patterns caused by solid particle impacts within a Francis turbine. The use of a reduced computational domain, excluding the spiral casing, proved effective in accurately reproducing the pressure distribution on the runner, significantly lowering computational costs without compromising hydrodynamic accuracy. The areas of highest erosion were identified on the rear face of the guide vanes and in the outlet region of the runner, particularly near the crown and band ring. These zones aligned with high-density particle trajectories impacting at angles and velocities known to intensify material damage, as predicted by the Oka model. The analysis revealed a predominant impact angle near 92°, consistent with severe erosion due to nearly normal impacts, and a velocity range mostly between 6 and 9 m/s—with occasional high-energy collisions up to 40 m/s contributing disproportionately to material loss.

Beyond confirming known erosion mechanisms, the methodology enabled the quantification of volumetric material loss per unit mass of impacting particles and the localization of critical erosion zones. These capabilities offer a robust foundation for evaluating alternative designs and mitigation strategies, such as protective coatings or hydraulic redesign. The results align with the existing literature and validate the applicability of the Oka model under real-world conditions involving high sediment loads, like those found in Andean hydroelectric systems. A key contribution of this study is the demonstration that reliable erosion predictions for large-scale Francis turbines can be achieved using a fully open-source workflow, combining OpenFOAM simulations and Python-based post-processing. This not only reduces licensing costs but also enhances the reproducibility and adaptability of the methodology for different turbine geometries and operating conditions. Future research may build on these findings to explore the influence of material properties, optimize runner and vane geometries, and assess the long-term effectiveness of erosion-mitigating techniques, contributing to more resilient and efficient hydraulic systems.

Author Contributions: Conceptualization, V.H.H. and M.P.-S.; methodology, M.N., J.G. and V.H.H.; software, M.N. and J.G.; validation, H.M.R.; formal analysis, M.N., J.G. and V.H.H.; investigation, J.G.; resources, H.M.R.; data curation, M.N., J.G. and V.H.H.; writing—original draft preparation, M.N., J.G. and V.H.H.; writing—review and editing, M.P.-S. and H.M.R.; visualization, V.H.H. and H.M.R.; supervision, M.P.-S.; project administration, M.P.-S. and V.H.H.; funding acquisition, M.P.-S. All authors have read and agreed to the published version of the manuscript.

Funding: This research was funded by the Escuela Politécnica Nacional through the research project PIIF-23-04: "Thermographic Study of the Influence of Temperature Variations in 3D Printing with Bowden Technology Applied to Automotive Components Printing". The authors acknowledge the financial support of the Foundation for Science and Technology (FCT) through the project UIDB/04625/2025 of the research unit CERIS, as well as they are grateful for the project HY4RES (Hybrid Solutions for Renewable Energy Systems) EAPA_0001/2022 from INTERREG ATLANTIC AREA PROGRAMME.

Data Availability Statement: Data supporting the findings of this study are available from the corresponding author upon request.

Conflicts of interest: The authors declare no conflicts of interest.

References

1. Graham, E.; Fulghum, N.; Altieri, K. *Global Electricity Review 2025*; Technical report; EMBER: London, UK, 2025.
2. Association, I.H. *2024 World Hydropower Outlook*; Technical report; International Hydropower Association: London, UK, 2024.
3. Naranjo-Silva, S.; Naranjo-Silva, S. A hydropower development perspective in Ecuador: Past, present, and future. *La Granja* **2025**, *39*, 63–77. https://doi.org/10.17163/lgr.n39.2024.04. 656.
4. Li, W.F.; Feng, J.J.; Wu, H.; Lu, J.L.; Liao, W.L.; Luo, X.Q. Numerical investigation of pressure fluctuation reducing in draft tube of Francis turbines. *Int. J. Fluid Mach. Syst.* **2015**, *8*, 202–208. https://doi.org/10.5293/IJFMS.2015.8.3.202.
5. Armijos, E.; Laraque, A.; Barba, S.; Bourrel, L.; Ceron, C.; Lagane, C.; Magat, P.; Moquet, J.S.; Pombosa, R.; Sondag, F.; et al. Yields of suspended sediment and dissolved solids from the Andean basins of Ecuador. *Hydrol. Sci. J.* **2013**, *58*, 1478–1494. https://doi.org/10.1080/02626667.2013.826359.
6. Levy, A.V. The solid particle erosion behavior of steel as a function of microstructure. *Wear* **1981**, *68*, 269–287. https://doi.org/10.1016/0043-1648(81)90177-0.
7. Noon, A.A.; Kim, M.H. Erosion wear on Francis turbine components due to sediment flow. *Wear* **2017**, *378–379*, 126–135. https://doi.org/10.1016/j.wear.2017.02.040.
8. Thapa, B.S.; Thapa, B.; Dahlhaug, O.G. Empirical modelling of sediment erosion in Francis turbines. *Energy* **2012**, *41*, 386–391. https://doi.org/10.1016/j.energy.2012.02.066.
9. Tarodiya, R.; Levy, A. Surface erosion due to particle-surface interactions—A review. *Powder Technol.* **2021**, *387*, 527–559 https://doi.org/10.1016/j.powtec.2021.04.055.
10. Oka, Y.I.; Okamura, K.; Yoshida, T. Practical estimation of erosion damage caused by solid particle impact: Part 1: Effects of impact parameters on a predictive equation. *Proc. Wear* **2005**, *259*, 95–101. https://doi.org/10.1016/j.wear.2005.01.039.
11. Wang, Y.; Tan, R.; Chang, B.; Chen, B.; Li, J.; Lu, Q.; Zhang, T. Simulation of Elbow Erosion of Gas–Liquid–Solid Three-Phase Shale Gas Gathering Pipeline Based on CFD-DEM. *Processes* **2024**, *12*, 1231. https://doi.org/10.3390/pr12061231.
12. Zhao, Y.; Zhang, K.; Guo, A.; Hao, F.; Ma, J. Predictive Model for Erosion Rate of Concrete Under Wind Gravel Flow Based on K-Fold Cross-Validation Combined with Support Vector Machine. *Buildings* **2025**, *15*, 614. https://doi.org/10.3390/buildings15040614.
13. Acharya, N.; Gautam, S.; Chitrakar, S.; Iliev, I.; Dahlhaug, O.G. Correlating Sediment Erosion in Rotary–Stationary Gaps of Francis Turbines with Complex Flow Patterns. *Energies* **2024**, *17*, 5961. https://doi.org/10.3390/en17235961.
14. He, S.; Song, X.; Wang, L.; Zhao, M.; Wang, Z. Numerical prediction of erosion of Francis turbine in sediment laden flow. *J. Phys. Conf. Ser.* **2024**, *2752*, 012204. https://doi.org/10.1088/1742-6596/2752/1/012204.
15. Shrestha, S.; Bijukchhe, P.L.; Poudel, R.; Chitrakar, S.; Thapa, B.; Guo, Z.; Qian, Z. Numerical Investigation of Sediment Erosion in Guide Vanes of Francis Turbine with Experimental Validations. *IOP Conf. Ser. Earth Environ. Sci.* **2024**, *1385*, 012008. https://doi.org/10.1088/1755-1315/1385/1/012008.
16. Cruzatty, C.; Jimenez, D.; Valencia, E.; Zambrano, I.; Mora, C.; Luo, X.; Cando, E. A case study: Sediment erosion in francis urbines operated at the san francisco hydropower plant in ecuador. *Energies* **2022**, *15*, 8. https://doi.org/10.3390/en15010008.
17. Wang, J.; Song, X.; Wang, J.; Wang, Z. Study on the Complex Erosion Characteristics and Specific Influencing Factor Mechanism in a Francis Hydraulic Turbine. *Water* **2025**, *17*, 1234. https://doi.org/10.3390/w17081234.
18. Xu, L.; Zhang, Q.; Zheng, J.; Zhao, Y. Numerical prediction of erosion in elbow based on CFD-DEM simulation. *Powder Technol.* **2016**, *302*, 236–246. https://doi.org/10.1016/j.powtec.2016.08.050.
19. Finnie, I. Erosion of surfaces by solid particles. *Wear* **1960**, *3*, 87–103. https://doi.org/10.1016/0043-1648(60)90055-7.
20. Tang, C.; Yang, Y.C.; Liu, P.Z.; Kim, Y.J. Prediction of abrasive and impact wear due to multi-shaped particles in a centrifugal pump via cfd-dem coupling method. *Energies* **2021**, *14*, 2391. https://doi.org/10.3390/en14092391.
21. Thapa, B.S.; Dahlhaug, O.G.; Thapa, B. Sediment erosion in hydro turbines and its effect on the flow around guide vanes of Francis turbine. *Renew. Sustain. Energy Rev.* **2015**, *49*, 1100–1113**.** https://doi.org/10.1016/j.rser.2015.04.178.
22. Gautam, S.; Acharya, N.; Chitrakar, S.; Neopane, H.P.; Iliev, I.; Dahlhaug, O.G. Sediment erosion in the labyrinths of Francis turbine: A numerical study. *IOP Conf. Ser. Earth Environ. Sci.* **2022**, *1037*, 012032. https://doi.org/10.1088/1755-1315/1037/1/012032.

23. Hutchings, I.; Shipway, P. *Tribology: Friction and Wear of Engineering Materials*, 2nd ed.; Butterworth-Heinemann: Oxford, UK, 2017.
24. Oka, Y.I.; Yoshida, T. Practical estimation of erosion damage caused by solid particle impact: Part 2: Mechanical properties of materials directly associated with erosion damage. *Wear* **2005**, *259*, 102–109. https://doi.org/10.1016/j.wear.2005.01.040.
25. Fortini, A.; Suman, A.; Zanini, N.; Cruciani, G. Erosive Wear Behavior of High-Chromium Cast Iron: Combined Effect of Erodent Powders and Destabilization Heat Treatments. *Coatings* **2022**, *12*, 1218. https://doi.org/10.3390/coatings12081218.
26. Shrestha, K.P.; Chitrakar, S.; Thapa, B.; Dahlhaug, O.G. Performance Comparison of Optimized Designs of Francis Turbines Exposed to Sediment Erosion in various Operating Conditions. *J. Phys. Conf. Ser.* **2018**, *1042*. https://doi.org/10.1088/1742-6596/1042/1/012001.
27. Liao, J.; Lai, X.; Zhang, X. Influence of particle diameters and concentration of sediment on internal flows in Francis turbine runners. *J. Hydroelectr. Eng.* **2017**, *36,* 88–94. https://doi.org/10.11660/slfdxb.20170510.
28. Singh, B.; Zafar, S. Microstructural and mechanical aspects of micrometric and nanometric Ni + 10. *J. Compos. Mater.* **2021**, *55*, 347–360. https://doi.org/10.1177/0021998320949617.
29. Parkash, O.; Kumar, A.; Sikarwar, B.S. Computational Erosion Wear Model Validation of Particulate Flow Through Mitre Pipe Bend. *Arab. J. Sci. Eng.* **2021**, *46*, 12373–12390. https://doi.org/10.1007/s13369-021-05931-x.
30. Narváez, M.; Cruzatty, C.; Valencia, E.; Hidalgo, V.; Luo, X.; Torres, A.; Erazo, J.; Altamirano, G.; Cando, E. Modeling of Solid Particle Erosion for a Water–Sand Impingement System Using OpenFOAM. *Coatings* **2023**, *13*, 2080. https://doi.org/10.3390/coatings13122080.
31. Arocena, V.M.; Danao, L.A.M. Improving the Modeling of Pressure Pulsation and Cavitation Prediction in a Double-Volute Double-Suction Pump Using Mosaic Meshing Technology. *Processes* **2023**, *11*, 660. https://doi.org/10.3390/pr11030660.
32. Montomoli, F.; Eastwood, S. Implementation of synthetic turbulence inlet for turbomachinery LES. *Comput. Fluids* **2011**, *46*, 369–374. https://doi.org/10.1016/j.compfluid.2010.11.019.
33. Salehi, S.; Nilsson, H. OpenFOAM for Francis Turbine Transients. *OpenFOAM® J.* **2021**, *1*, 47–61. https://doi.org/10.51560/ofj.v1.26.
34. Schlipf, M.; Tismer, A.; Riedelbauch, S. On the application of hybrid meshes in hydraulic machinery CFD simulations. *IOP Conf. Ser. Earth Environ. Sci.* **2016**, *49*, 062013. https://doi.org/10.1088/1755-1315/49/6/062013.
35. Chen, X.; Liu, J.; Pang, Y.; Chen, J.; Chi, L.; Gong, C. Developing a new mesh quality evaluation method based on convolutional neural network. *Eng. Appl. Comput. Fluid Mech.* **2020**, *14*, 391–400. https://doi.org/10.1080/19942060.2020.1720820.
36. Zaza, D.; Iovieno, M. On the Preferential Concentration of Particles in Turbulent Channel Flow: The Effect of the Added-Mass Factor. *Energies* **2024**, *17*, 783. https://doi.org/10.3390/en17040783.
37. Gong, Z.; Wu, Z.; An, C.; Zhang, B.; Fu, X. CP3d: A comprehensive Euler-Lagrange solver for direct numerical simulation of particle-laden flows. *Comput. Phys. Commun.* **2023**, *286*, 108666. https://doi.org/10.1016/j.cpc.2023.108666.
38. Speziale, C.G.; Thangam, S. Analysis of an RNG based turbulence model for separated flows. *Int. J. Eng. Sci.* **1992**, *30*, 1379–IN4. https://doi.org/10.1016/0020-7225(92)90148-A.
39. Pineda, P.; Iranzo, A. Analysis of sand-loaded air flow erosion in heritage sites by Computational Fluid Dynamics: Method and damage prediction. *J. Cult. Herit.* **2017**, *25*, 75–86. https://doi.org/10.1016/j.culher.2016.12.005.
40. Lira, S.H.; Torres, M.J.; Silva, R.G.; Viñuela, J.Z. Numerical characterization of the solid particle accumulation in a turbulent flow through curved pipes by means of Stokes numbers. *Appl. Sci.* **2021**, *11*, 7381. https://doi.org/10.3390/app11167381.
41. H K, V.; Malalasekera, W. *Introduction: Computational Fluid Dynamics. The Finite Volume Method*; Prentice Hall: Hoboken, NJ, USA, 2006; Volume 44.
42. Ferziger, J.H.; Perić, M.; Street, R.L. *Computational Methods for Fluid Dynamics*, 4th ed.; Springer: Cham, Switzerland, 2019. https://doi.org/10.1007/978-3-319-99693-6.
43. Tominaga, Y. Flow around a high-rise building using steady and unsteady RANS CFD: Effect of large-scale fluctuations on the velocity statistics. *J. Wind Eng. Ind. Aerodyn.* **2015**, *142*, 93–103. https://doi.org/10.1016/j.jweia.2015.03.013.
44. Sommerfeld, M. Validation of a stochastic Lagrangian modelling approach for inter-particle collisions in homogeneous isotropic turbulence. *Int. J. Multiph. Flow* **2001**, *27*, 1829–1858. https://doi.org/10.1016/S0301-9322(01)00035-0.
45. Hidalgo, V.; Velasco, M.; Cando, E.; Valencia, E.; Simbaña, S.; Puga, D.; Mora, C.; Escaler, X. Rotatory 3D structured mesh study using openFOAM to simulate the flow in francis turbine. *Mater. Today Proc.* **2022**, *49*, 142–148. https://doi.org/https://doi.org/10.1016/j.matpr.2021.07.492.
46. Cruz, L.M.D.L. MQ-RBF Meshless Method for solving CFD problems using an Object-Oriented Approach. *SCAT Mobility Grant Report.* **2008**, *1*, 1.

47. Xiao, H.; Sun, J. Algorithms in a robust hybrid CFD-DEM solver for particle-laden flows. *Commun. Comput. Phys.* **2011**, *9*, 297–323. https://doi.org/10.4208/cicp.260509.230210a.
48. Anagnostopoulos, J.S.; Papantonis, D.E. Flow Modeling and Runner Design Optimization in Turgo Water Turbines. *Int. J. Mech. Aerosp. Ind. Mechatron. Eng.* **2007**, *1, 183-188*.
49. Haspel, N.; Mayer, J.F.; Stoner, H. Prediction of inviscid flow in axial turbines in comparison with measurements. *ASME 1993 Int. Gas Turbine Aeroengine Congr. Expo.* **1993**, *1,* V001T03A053. https://doi.org/10.1115/93-GT-112.
50. Riber, E.; Moureau, V.; García, M.; Poinsot, T.; Simonin, O. Evaluation of numerical strategies for large eddy simulation of particulate two-phase recirculating flows. *J. Comput. Phys.* **2009**, *228*, 539–564. https://doi.org/10.1016/j.jcp.2008.10.001.
51. Karunarathne, S.S.; Tokheim, L.A. Comparison of the influence of drag models in CFD simulation of particle mixing and segregation in a rotating cylinder. *Linköping Electron. Conf. Proc.* **2017**, *138*, 151–156. https://doi.org/10.3384/ecp17138151.
52. Santos, D.S.; Garcia, F.; Rasteiro, M.; Faia, P. Oil/water flow in a horizontal pipe-dispersed flow regime. *Int. J. Comput. Methods Exp. Meas.* **2020**, *8*, 123–134. https://doi.org/10.2495/CMEM-V8-N2-123-134.
53. Hu, R.; Liu, Y.; Ravnik, J.; Hriberšek, M.; Steinmann, P.; Cui, Y. A hybrid analytical–numerical model for calculating the maximum elastic force acting on a flow-driven elastic prolate spheroidal particle during its collision with a rigid wall. *Comput. Mech.* **2022**, *69*, 1021–1029. https://doi.org/10.1007/s00466-021-02127-w.
54. Shrestha, R.; Shrestha, K.; Chitrakar, S.; Thapa, B.; Neopane, H.P.; Qian, Z.; Guo, Z. Evaluation of different erosion models for predicting guide vane wear in Francis turbine. *Front. Mech. Eng.* **2025**, *11*, 1542074
55. Oka, Y.; Ohnogi, H.; Hosokawa, T.; Matsumura, M. The impact angle dependence of erosion damage caused by solid particle impact. *Wear* **1997**, *203–204*, 573–579. https://doi.org/10.1016/S0043-1648(96)07430-3.
56. Umar, B.; Huang, X. Numerical Investigation of Performance and Flow Characteristics of Francis Turbine in Part Load Condition. *J. Phys. Conf. Ser.* **2024**, *2752*, 012006. https://doi.org/10.1088/1742-6596/2752/1/012006.
57. Umar, B.M.; Wang, Z.; Chitrakar, S.; Thapa, B.; Huang, X.; Poudel, R.; Karna, A. Experimental Erosion Flow Pattern Study of Pelton Runner Buckets Using a Non-Recirculating Test Rig. *Energies* **2024**, *17*, 4006. https://doi.org/10.3390/en17164006.